THERMAL SIGNATURES OF TETHER-CUTTING RECONNECTIONS IN PRE-ERUPTION CORONAL FLUX ROPES: HOT CENTRAL VOIDS IN CORONAL CAVITIES

Y. FAN
High Altitude Observatory, National Center for Atmospheric Research, 3080 Center Green Drive, Boulder, CO 80301, USA

ABSTRACT

Using a three-dimensional MHD simulation, we model the quasi-static evolution and the onset of eruption of a coronal flux rope. The simulation begins with a twisted flux rope emerging at the lower boundary and pushing into a pre-existing coronal potential arcade field. At a chosen time the emergence is stopped with the lower boundary taken to be rigid. Then the coronal flux rope settles into a quasi-static rise phase during which an underlying, central sigmoid-shaped current layer forms along the so-called hyperbolic flux tube (HFT), a generalization of the X-line configuration. Reconnections in the dissipating current layer effectively add twisted flux to the flux rope and thus allow it to rise quasi-statically, even though the magnetic energy is decreasing as the system relaxes. We examine the thermal features produced by the current layer formation and the associated "tether-cutting" reconnections as a result of heating and field aligned thermal conduction. It is found that a central hot, low-density channel containing reconnected, twisted flux threading under the flux rope axis forms on top of the central current layer. When viewed in the line of sight roughly aligned with the hot channel (which is roughly along the neutral line), the central current layer appears as a high-density vertical column with upward extensions as a "U"-shaped dense shell enclosing a central hot, low-density void. Such thermal features have been observed within coronal prominence cavities. Our MHD simulation suggests that they are the signatures of the development of the HFT topology and the associated tether-cutting reconnections, and that the central void grows and rises with the reconnections, until the flux rope reaches the critical height for the onset of the torus instability and dynamic eruption ensues.

Key words: magnetic fields – magnetohydrodynamics (MHD) – methods: numerical – Sun: activity – Sun: corona – Sun: coronal mass ejections (CMEs)

Online-only material: animations

1. INTRODUCTION

Coronal mass ejections (CMEs) and eruptive flares are believed to result from a sudden, explosive release of the free magnetic energy stored in the previously quasi-equilibrium, twisted/sheared coronal magnetic field (see, e.g., reviews by Forbes et al. 2006; Chen 2011). Many CME models have considered a magnetic flux rope containing helical field lines twisting about each other in the corona as the basic underlying magnetic field structure for CME precursors (e.g., Titov & Demoulin 1999; Low 2001; Gibson & Fan 2006). Recent observational studies of coronal prominence cavities support the picture of twisted coronal flux ropes as CME precursors (e.g., Wang & Stenborg 2010). Theoretical studies have shown that a coronal flux rope confined by an external potential magnetic field can become unstable to the torus instability and erupt when it reaches a critical height where the ambient potential field decreases with height too steeply (Kliem & Török 2006; Isenberg & Forbes 2007; Démoulin & Aulanier 2010). MHD simulations have been carried out to study the critical condition and the nonlinear evolution of the torus instability of various three-dimensional (3D) coronal flux rope structures (e.g., Török & Kliem 2007; Fan & Gibson 2007; Aulanier et al. 2010; Fan 2010).

Through a sequence of 3D MHD simulations of the evolution of the coronal magnetic field resulting from the emergence of a twisted magnetic flux rope into a pre-existing coronal arcade field, Fan (2010) studied the conditions that lead to a dynamic eruption of the resulting coronal flux rope. It is found that the critical condition for the onset of eruption is for the center of the flux rope to reach a critical height at which the corresponding

potential field declines with height at a sufficiently steep rate, consistent with the onset of the torus instability of the flux rope. The simulations show that after the flux emergence is stopped, the coronal flux rope first settles into a quasi-static rise phase with an underlying, central sigmoid-shaped current layer developing. Reconnections in the current layer are found to effectively add twisted flux to the flux rope (as quantified by Equation (14) in Fan 2010), allowing it to rise quasi-statically, even as the magnetic energy is declining. We thus call these reconnections "tether-cutting" reconnections in the sense that they are effectively reducing the anchoring of the flux rope by dissipating the underlying, central current layer whose current attracts the volume current in the flux rope (Low & Zhang 2002). When the flux rope rises quasi-statically to the critical height for the onset of the torus instability, then dynamic eruption ensues. To identify the thermal signatures that may result from the formation of the current layer and the associated reconnections, we carry out an MHD simulation with a similar setup as those in Fan (2010), but with a more sophisticated treatment of the thermodynamics. Instead of assuming a simple isothermal evolution, we solve the total energy equation in conservative form for a perfect gas with an adiabatic index $\gamma = 1.1$. In this way, the non-adiabatic heating due to the dissipation of kinetic and magnetic energies by the numerical diffusions is implicitly incorporated in the thermal energy. Also thermal conduction along the magnetic field lines is included in the energy equation. We find from this new simulation that the main consequence of the tether-cutting reconnections in the current layers during the quasi-static phase is the formation and enlargement of a hot, low-density channel, containing reconnected, twisted flux threading under the axis of the flux rope. When viewed above the limb

along a line of sight that is roughly aligned with the channel, the thermal signature would manifest in *SDO*/AIA observations as a hot central void enclosed in a "U"-shaped dense shell on top of a relatively dense structure inside the flux rope. This signature inside the flux rope is consistent with the recent observations of the thermal sub-structures inside coronal prominence cavities by Reeves et al. (2012), Berger (2012), and Régnier et al. (2011).

We organize the remainder of the paper as follows. In Section 2, we describe the MHD numerical model with the more sophisticated treatment of the thermodynamics compared to the previous simulations in Fan (2010). In Section 3, we describe the simulation result, focusing on the thermal signature that develops inside the flux rope and compare it with observations. We summarize and discuss the conclusions in Section 4.

2. MODEL DESCRIPTION

For the simulation carried out in this study, we solve the following magneto-hydrodynamic equations in a spherical domain:

$$\frac{\partial \rho}{\partial t} + \nabla \cdot (\rho \mathbf{v}) = 0, \tag{1}$$

$$\rho \left(\frac{\partial \mathbf{v}}{\partial t} + (\mathbf{v} \cdot \nabla)\mathbf{v} \right) = -\nabla p - \rho \frac{GM_\odot}{r^2}\hat{\mathbf{r}} + \frac{1}{4\pi}(\nabla \times \mathbf{B}) \times \mathbf{B}, \tag{2}$$

$$\frac{\partial \mathbf{B}}{\partial t} = \nabla \times (\mathbf{v} \times \mathbf{B}), \tag{3}$$

$$\nabla \cdot \mathbf{B} = 0, \tag{4}$$

$$\frac{\partial e}{\partial t} = -\nabla \cdot \left[\left(\varepsilon + \rho \frac{v^2}{2} + p \right) \mathbf{v} - \frac{1}{4\pi}(\mathbf{v} \times \mathbf{B}) \times \mathbf{B} \right]$$
$$- \rho \mathbf{v} \cdot \frac{GM_\odot}{r^2}\hat{\mathbf{r}} - \nabla \cdot \mathbf{q}, \tag{5}$$

$$p = \frac{\rho R T}{\mu}, \tag{6}$$

where

$$\varepsilon = \frac{p}{\gamma - 1}, \tag{7}$$

$$e = \varepsilon + \rho \frac{v^2}{2} + \frac{B^2}{8\pi}, \tag{8}$$

$$\mathbf{q} = -\kappa_0 T^{5/2}\hat{\mathbf{b}}\hat{\mathbf{b}} \cdot \nabla T. \tag{9}$$

In the above, $\mathbf{v}$ is the velocity field; $\mathbf{B}$ is the magnetic field; ρ, p, and T are, respectively, the plasma density, pressure, and temperature; ε, e, R, μ, and γ are, respectively, the internal energy density, the total energy density (internal+kinetic+magnetic), the gas constant, the mean molecular weight, and the adiabatic index of the perfect gas; $\mathbf{q}$ is the heat flux due to field aligned thermal conduction, with the field direction denoted by the unit vector $\hat{\mathbf{b}}$ and with $\kappa_0 = 10^{-6}$ erg $K^{-7/2}$ cm^{-1} s^{-1}; and G and $M_\odot$ denote the gravitational constant and the mass of the Sun. We have assumed a perfect gas with a low value of the adiabatic index: $\gamma = 1.1$, which allows the coronal plasma to better maintain its (high) temperature during adiabatic expansion. No *explicit* viscosity and magnetic diffusion are included in the momentum and the induction equations. However numerical dissipations are present at regions of sharp gradient, and since we are

solving the total energy equation of the plasma in conservative form (Equation (5)), the non-adiabatic heating due numerical dissipation of kinetic and magnetic energies is implicitly put back into the internal energy. We also explicitly include the non-adiabatic effect due to the field-aligned thermal conduction (Equations (5) and (9)) in the energy equation, but in a limited way. Given the temperature and density in the solar corona, the field aligned thermal conduction would pose a severe limit on the time step of numerical integration. Here, we artificially limit the conductive heat flux by limiting $(\gamma - 1)(m_p/2k\rho)\kappa_0 T^{5/2}$ to a maximum value of $\delta x^2/(8\,\delta t)$, where m_p is the proton mass, k is the Boltzmann constant, δx is the smallest dimension of the grid cell, and δt is the numerical time step calculated from the Courant condition based on all the other dynamical terms. Note that this limiting is a purely numerical consideration to avoid the extremely stringent time step that would be required by the Courant condition set by the thermal diffusion at large r where density decreases rapidly. This limiting is mainly altering thermal conduction in the region above $r = 1.4\,R_\odot$ to reduce it such that the time step set by the Courant condition for the thermal diffusion does not go below that set by the fastest dynamical speed. Since we are focusing on the thermal signatures that develop during the quasi-static phase over a timescale long compared to the dynamic timescale and inside the flux rope below $r = 1.4\,R_\odot$ where the thermal conduction is unaltered, we do not expect this limiting of thermal conduction to significantly alter the qualitative properties of the thermal signatures. Thus with the present treatment of the thermodynamics, we aim to *qualitatively* identify regions of significant heating due to the formation and dissipation of current layers and the resulting regions of enhanced temperature with the redistribution of heat by the field aligned thermal conduction.

We solve the above compressible MHD equations using a numerical code which has its origin from the ZEUS3D code of Stone & Norman (1992a, 1992b), but has been substantially modified and rewritten, in particular in the schemes used to solve the continuity, the momentum, and the energy equations, and in the scheme for time stepping (Fan 2009, 2011). For ease of future reference, we call this code "MFE" standing for "Magnetic Flux Eruption," since it has been mainly used for modeling flux emergence from the interior into the solar atmosphere and corona in Cartesian geometry (Fan 2009), and for modeling CME initiation in the corona in spherical geometry (Cottaar & Fan 2009; Fan 2010, 2011). Here, we summarize the numerical schemes used by the MFE code for solving the above MHD equations. The dependent field variables are discretized using a staggered mesh in the spherical domain with r, θ, ϕ coordinates (Stone & Norman 1992a). A modified, second-order accurate Lax–Friedrichs scheme described in Rempel et al. (2009, see Equation (A3) in that paper) is applied for evaluating the fluxes in the continuity and the energy equations. The standard second-order Lax–Friedrichs scheme is used for evaluating the fluxes in the momentum equation. A method of characteristics that is upwind in the Alfvén waves (Stone & Norman 1992b) is used for evaluating the $\mathbf{v} \times \mathbf{B}$ term in the induction equation, together with the constrained transport scheme to ensure $\nabla \cdot \mathbf{B} = 0$ to the machine precision. For temporal discretization, the code uses a second-order accurate predictor-corrector time stepping. The thermal conduction term is treated via an operator splitting procedure as follows. All the other equations and the total energy equation (Equation (5)) excluding the thermal conduction term are first advanced one full time step (with the second-order predictor-corrector time stepping). Then a separate step (with
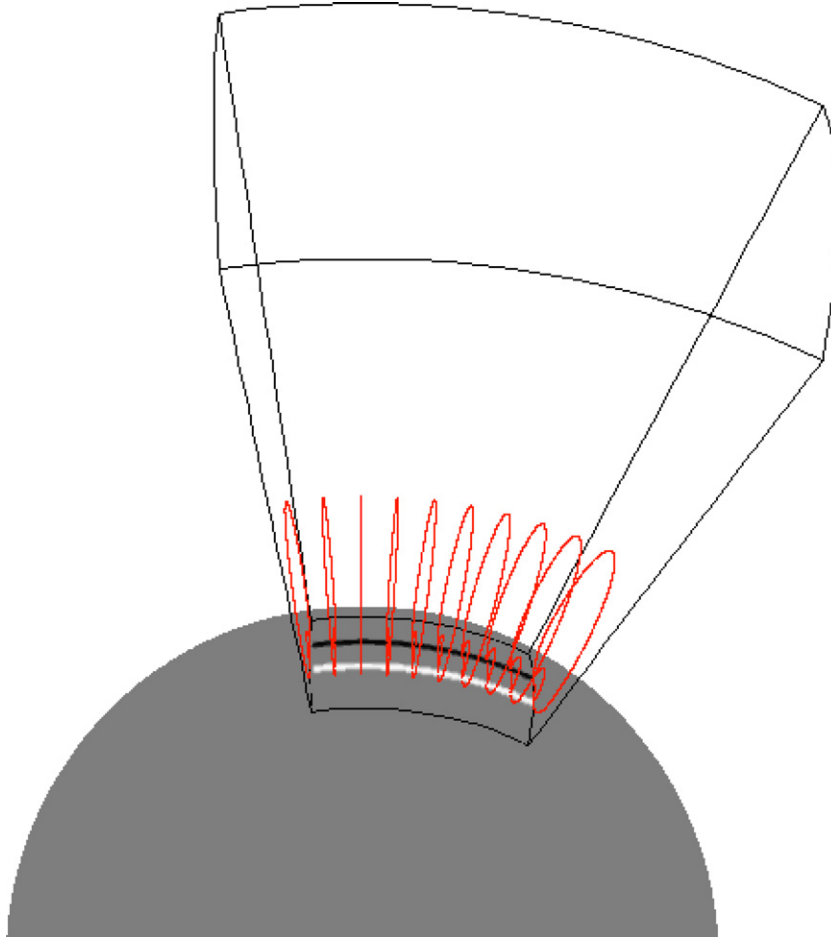
Figure 1. Initial configuration of the simulation, same as that used in Fan (2010), See the text for details.

(An animation of this figure is available in the online journal.)

a second-order predictor-corrector time stepping) is carried out to further update the internal energy for the thermal conduction term and adjust the total energy accordingly.

The initial set up of the simulation is the same as that of Fan (2010). The spherical domain (see Figure 1) representing the corona is given by $r \in [R_\odot, 5.496\, R_\odot]$, $\theta \in [5\pi/12, 7\pi/12]$, and $\phi \in [-\pi/9.6, \pi/9.6]$, where $R_\odot$ is the solar radius. It is resolved by a grid of $432 \times 192 \times 240$, which is uniform in θ and ϕ, and non-uniform in r: in the range from $r = R_\odot$ to $r = 1.788\, R_\odot$, the grid size is $dr = 0.0027271\, R_\odot = 1.898$ Mm, and dr increases gradually for $r > 1.788\, R_\odot$, reaching about $dr = 0.09316\, R_\odot$ at the outer boundary.

Initially, the domain is assumed to be in hydrostatic equilibrium at a uniform temperature of $T_0 = 1$ MK with the density and pressure given by

$$\rho = \rho_0 \exp\left(-\frac{R_\odot}{H_{p0}}\left(1 - \frac{R_\odot}{r}\right)\right) \quad (10)$$

$$p = \frac{RT_0\rho}{\mu}, \quad (11)$$

where $\rho_0 = 8.365 \times 10^{-16}$ g cm^{-3} is the initial density at the coronal base and $H_{p0} = (RT_0/\mu)(GM_\odot/R_\odot^2)^{-1}$ denotes the initial pressure scale height, which is about 60 Mm. The initial atmosphere contains a pre-existing potential arcade field, whose normal field $B_r(0, \theta)$ at the lower boundary (see the gray-scale

image on the sphere in Figure 1) is given by

$$B_r(0, \theta) = \frac{1}{R_\odot^2 \sin\theta}\frac{dA_s(\theta)}{d\theta}, \quad (12)$$

where

$$A_s(\theta)$$

$$= \begin{cases} 0, & \dfrac{5}{12}\pi < \theta < \dfrac{\pi}{2} - \theta_t - \theta_a, \\[2mm] -\dfrac{\theta_a}{\pi}\sin\theta_p B_0 R_\odot^2\left[1 - \cos\left[\dfrac{\pi}{\theta_a}\left[\theta - \left(\dfrac{\pi}{2} - \theta_a - \theta_t\right)\right]\right]\right], & \\[1mm] & \dfrac{\pi}{2} - \theta_t - \theta_a < \theta < \dfrac{\pi}{2} - \theta_t, \\[2mm] -\dfrac{2\theta_a}{\pi}\sin\theta_p B_0 R_\odot^2, & \dfrac{\pi}{2} - \theta_t < \theta < \dfrac{\pi}{2} + \theta_t, \\[2mm] -\dfrac{\theta_a}{\pi}\sin\theta_p B_0 R_\odot^2\left[1 + \cos\left[\dfrac{\pi}{\theta_a}\left[\theta - \left(\dfrac{\pi}{2} + \theta_t\right)\right]\right]\right], & \\[1mm] & \dfrac{\pi}{2} + \theta_t < \theta < \dfrac{\pi}{2} + \theta_t + \theta_a, \\[2mm] 0, & \dfrac{\pi}{2} + \theta_t + \theta_a < \theta < \dfrac{7}{12}\pi, \end{cases} \quad (13)$$

in which $\theta_a = 0.05$, $\theta_t = 0.0432$, $\theta_p = \pi/2 - \theta_t - \theta_a/2$, and $B_0 = 20$ G is the peak field strength in the arcade field. Thus, the peak Alfvén speed at the footpoint of the arcade field is

$v_{A0} = B_0/\sqrt{4\pi\rho_0} = 1951$ km s^{-1} which is more than a factor of 10 greater than the initial sound speed of 135 km s^{-1}.

As in Fan (2010), we impose (kinematically) at the lower boundary of the domain (at $r = R_\odot$) the emergence of a twisted magnetic torus $\mathbf{B}_{\rm tube}$, by specifying a time-dependent transverse electric field $\mathbf{E}_\perp|_{r=R_\odot}$ that corresponds to the upward advection of the flux tube at a velocity $\mathbf{v}_0$:

$$\mathbf{E}_\perp|_{r=R_\odot} = \hat{\mathbf{r}} \times \left[\left(-\frac{1}{c}\mathbf{v}_0 \times \mathbf{B}_{\rm tube}(R_\odot, \theta, \phi, t) \right) \times \hat{\mathbf{r}} \right]. \quad (14)$$

Here, the imposed velocity field on the lower boundary is a constant $\mathbf{v}_0$ in the area where the emerging tube intersects the lower boundary and zero in the rest of the area. The field structure $\mathbf{B}_{\rm tube}$ used for specifying $\mathbf{E}_\perp|_{r=R_\odot}$ is an axisymmetric torus defined in its own local spherical polar coordinate system (r', θ', ϕ') whose origin is located at $\mathbf{r} = \mathbf{r}_0 = (r_0, \theta_0, \phi_0)$ of the Sun's spherical coordinate system and whose polar axis is parallel to the polar axis of the Sun's spherical coordinate system:

$$\mathbf{B}_{\rm tube} = \nabla \times \left(\frac{A(r', \theta')}{r'\sin\theta'}\hat{\phi}' \right) + B_{\phi'}(r', \theta')\hat{\phi}', \quad (15)$$

where

$$A(r', \theta') = \frac{1}{2}qa^2 B_t \exp\left(-\frac{\varpi^2(r', \theta')}{a^2} \right), \quad (16)$$

$$B_{\phi'}(r', \theta') = \frac{aB_t}{r'\sin\theta'} \exp\left(-\frac{\varpi^2(r', \theta')}{a^2} \right), \quad (17)$$

where a is the minor radius of the torus, $\varpi = (r'^2 + R'^2 - 2r'R'\sin\theta')^{1/2}$ is the distance to the curved axis of the torus, with R' being the major radius of the torus, q denotes the angle (in rad) of field line rotation about the axis over a distance a along the axis, and $B_t a/R'$ gives the field strength at the curved axis of the torus. Here we have $a = 0.04314\,R_\odot$, $R' = 0.25\,R_\odot$, $q/a = -0.0166$ rad Mm^{-1}, and $B_t a/R = 2.24 B_0$. The magnetic field $\mathbf{B}_{\rm tube}$ is truncated to zero outside of the flux surface whose distance to the torus axis is $\varpi = a$. For specifying the flux emergence via $\mathbf{E}_\perp|_{r=R_\odot}$ given by Equation (14), it is assumed that the torus' center is initially located at $\mathbf{r}_0 = (r_0 = 0.707\,R_\odot, \theta_0 = \pi/2, \phi_0 = 0)$ (thus the torus is initially entirely below the surface) and it moves bodily toward the lower boundary at a constant velocity $\mathbf{v}_0 = v_0\hat{\mathbf{r}}_0$, with $v_0 = 0.001 v_{A0}$, until a time $t_{\rm stp}$, when the emergence is stopped and $\mathbf{E}_\perp|_{r=R_\odot}$ is set to zero. During flux emergence, we assume that the density inside the emerging flux tube is uniformly ρ_0 (same as the initial density at the bottom of the domain). Thus, as the tube is being transported into the domain via the electric field at the lower boundary, there is also an inflow of mass flux $\rho_0 v_{0r}$ through the lower boundary in the area where the emerging tube intersects the boundary. When the emergence is stopped, both the electric field and the velocity at the lower boundary are set to zero, with no inflows or outflows and with field line footpoints rigidly anchored. We assume perfectly conducting walls for the side boundaries of the simulation domain. For the outer boundary, we use a simple outward extrapolating boundary condition that allows plasma and magnetic field to flow through. These boundary conditions described above are the same as those used in Fan (2010)

For the present simulation, we drive the emergence of the torus via the electric field at the lower boundary until $t_{\rm stp} =$ 90 $R_\odot/v_{A0}$, the same as case e4 in Fan (2010). However, the difference between this simulation and those in Fan (2010) is that here we no longer assume the simple isothermal evolution, but instead we solve the total energy equation for a perfect gas with an adiabatic index $\gamma = 1.1$ for the coronal plasma. Thus, we take into account non-adiabatic effects due to heating produced by (numerical) dissipation of kinetic and magnetic energies. We also incorporate thermal conduction along the magnetic field lines, as is described earlier in Section 2. Thus, temperature can vary due to adiabatic expansion/compression, as well as due to the non-adiabatic effects: heating and thermal conduction. This enables us to identify sites of significant heating due to current sheet formation and study the resultant temperature distribution (qualitatively) during the evolution of the 3D flux rope in the corona.

3. RESULTS

Figure 2 shows snapshots of the 3D evolution of the coronal magnetic field after the imposed flux emergence at the lower boundary has stopped at $t_{\rm stp} = 90\,R_\odot/v_{A0} = 8.92$ hr. Figure 3 shows the temporal evolution of the rise speed at the apex of the tracked axis of the emerged flux rope (upper panel) and the total magnetic energy in the coronal domain (lower panel) after $t_{\rm stp}$. The way we track the axis of the emerged flux rope is the same as that described in Fan (2010, see discussion under Figure 3 in that paper). We find that the flux rope first settles into a phase of quasi-static rise, and then begins to accelerate and erupt when a critical height of roughly $1.25\,R_\odot$ is reached by the tube axis. During the quasi-static phase after the emergence is stopped, there is no more input of Poynting flux from the lower boundary and the magnetic energy in the domain is slowly decreasing (see Figure 3) due to tether-cutting reconnections in the current sheets that develop, as we will discussed later. Compared to the corresponding case e4 in Fan (2010) with the same imposed lower boundary conditions, the present case with a different treatment of the thermodynamics is found to undergo a longer quasi-static rise phase before the flux rope reaches roughly the same critical height for the onset of the torus instability. As a result, at the time of the onset of eruption, the (free) magnetic energy is lower and the Alfvén speed at the rope axis is also lower (by about 15%) in the present case. Thus, it is found that the eruption is slightly less energetic with the flux rope accelerating to a lower peak speed of about 371 km s^{-1} for the eruption, compared to the peak speed of about 429 km s^{-1} in the corresponding e4 case in Fan (2010). Here, we focus on studying the development of the thermal signatures in the flux rope as a result of current sheet formation and tether-cutting reconnections during the quasi-static rise phase. The tether-cutting reconnections after the emergence is stopped continue to build up the twisted flux of the flux rope (as computed in Equations (14) in Fan 2010), even no more Poynting flux is coming through the lower boundary and the magnetic energy is declining. They enable the flux rope to reach the critical height and eventually erupt. Therefore, the thermal structures that develop due to the reconnections may be important signatures for indicating the readiness of the flux rope to erupt, and identifying such thermal signatures in the observables is useful.

Figure 4 shows snapshots of the density (in log scale), current density normalized by magnetic field strength ($J/B \equiv |\nabla \times \mathbf{B}|/B$), and temperature in the central meridional cross-section of the flux rope shown in the corresponding snapshots in Figure 2. In the density cross-section during the quasi-static
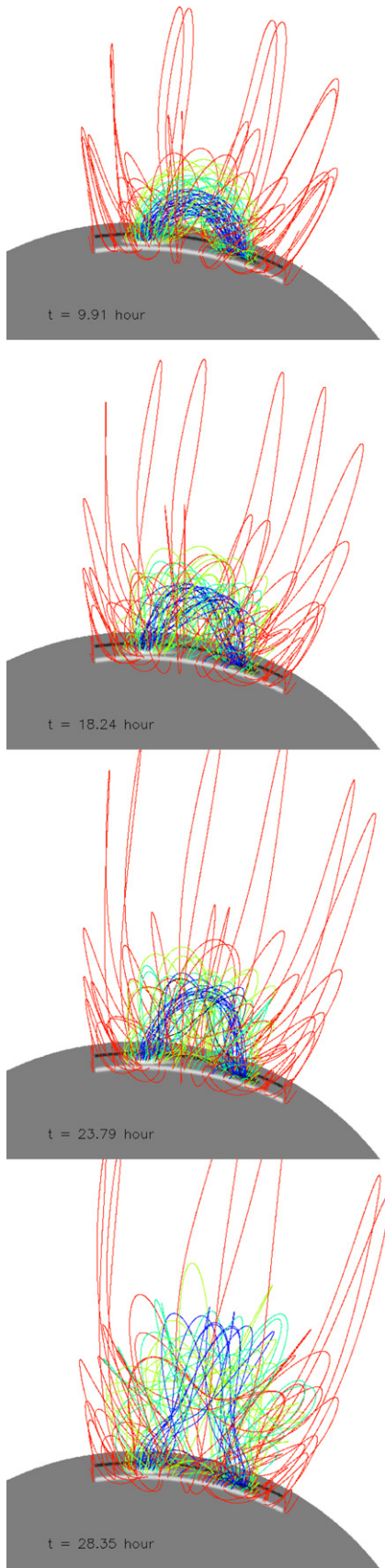
Figure 2. Snapshots of the 3D coronal magnetic field lines after the imposed flux emergence is stopped. A movie of the magnetic field evolution together with the evolution shown in Figure 4 below is also available in the electronic version of the paper.
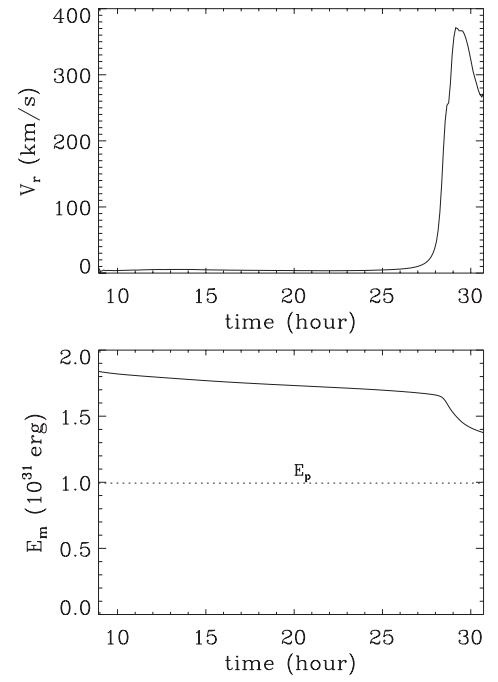

Figure 3. Rise velocity at the apex of the tracked axis of the emerged flux rope (upper panel) and the total magnetic energy E_m in the simulation domain (lower panel) as a function of time after the imposed flux emergence has stopped. The dotted line marks the magnetic energy of the corresponding potential field, E_p, which remains unchanged after the emergence has stopped. The eruption causes a roughly 43% reduction of the free magnetic energy.

rise phase (panels in the left column), the outermost low-density layer corresponds to the pre-existing arcade fields, and the low density is produced by the stretching and expansion of the pre-existing arcade fields immediately surrounding the emerged flux rope fields. Inside the outermost low-density layer is a layer of relatively high density and high J/B (indicated by the yellow arrows in Figure 4), which corresponds to the outer boundary of the emerged flux rope. Inside the flux rope, there is a central low-density void (indicated by the green arrows in Figure 4) which grows in size during the quasi-static phase. The central void is closed at the bottom with a sharp U-shaped lower boundary, and is enclosed in a high-density shell. The sharp lower boundary of the void corresponds to a U-shaped current concentration of high J/B which extends from a strong central vertical current layer below (see the middle and bottom snapshots in the second column of Figure 4). In other words, the central void is shaped like a "lollipop" on top of a vertical "stick" corresponding to the central vertical current layer, and the current layer extends upward to surround the two sides of the void. The middle and lower images in the right column of Figure 4 show that the central growing void is the hottest part in the central meridional cross-section, hotter than the plasma in the strongest vertical current layer below it and the current layer surrounds it. Furthermore, this hot void is growing below the apex of the emerged flux rope axis marked with the yellow "x" point in the cross-sections shown in Figure 4.

Figure 5 shows the 3D coronal field lines and the isosurface of J/B at a value of $1/(10\,dr)$ where dr is the smallest grid size in r. We find that at $t = 9.91$ hr, corresponding to the top row of Figure 4, the strongest portions of the current layers are two J-shaped layers curving about the two legs of the flux rope at the boundaries between the flux rope legs and the arcade with the opposite polarity footpoints. This is why the central
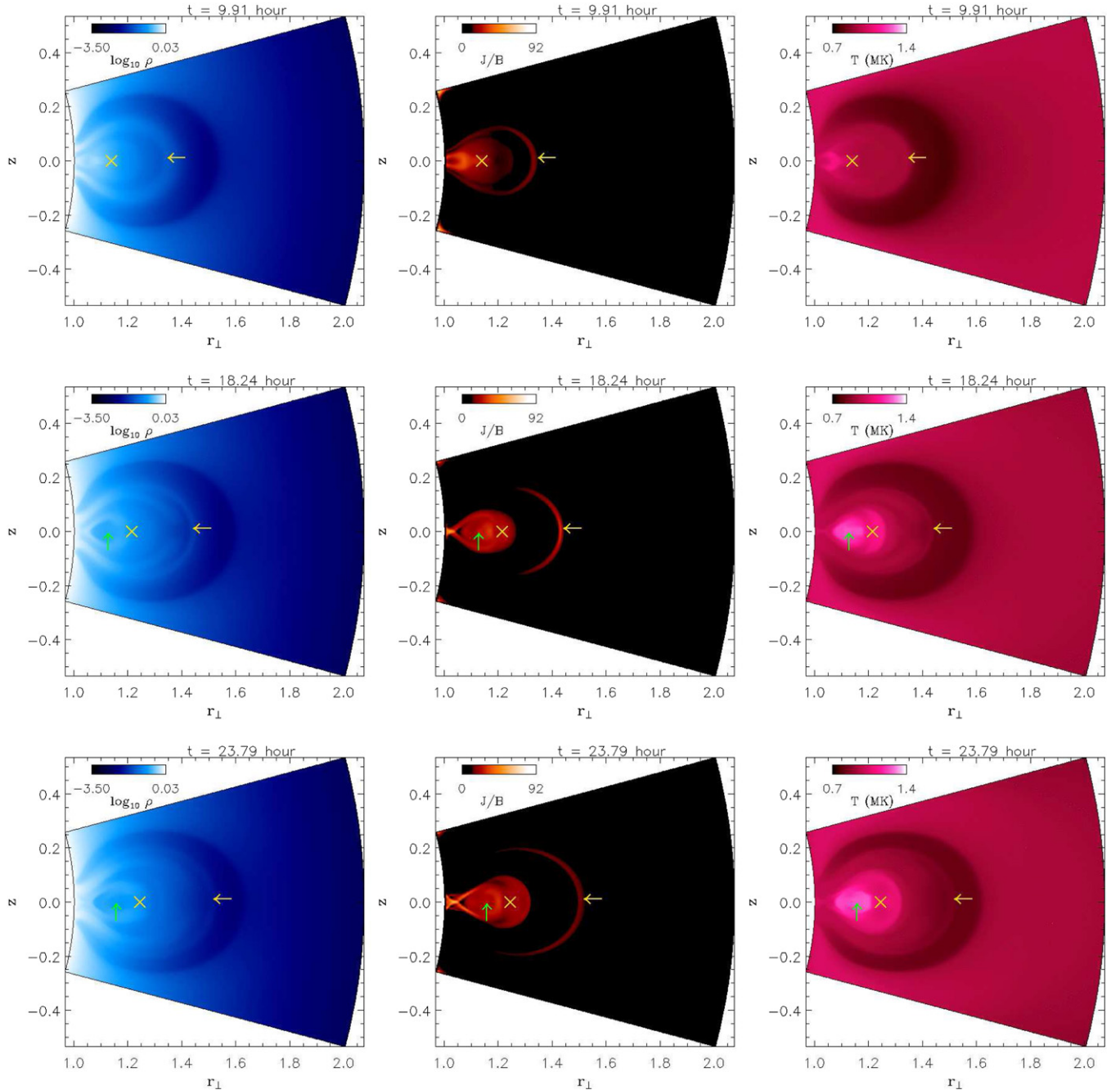
Figure 4. Snapshots of the density (in log scale), current density normalized by magnetic field strength ($J/B \equiv |\nabla \times \mathbf{B}|/B$), and temperature in the central meridional cross-section of the flux rope shown in the corresponding snapshots in Figure 2. Here, the density is in units of $\rho_0 = 8.365 \times 10^{-16}$, and J/B is in units of $1/R_\odot$. The features indicated by the green and the yellow arrows and the yellow "X" points are discussed in the text. A movie of the evolution shown in this figure together with the evolution shown in Figure 2 is also available in the online version of the paper.

(An animation of this figure is available in the online journal.)

meridional cross-section of J/B (the top panel in the middle column of Figure 4) shows a double-legged structure, with each leg belonging to one of the J-layers. When the lollipop-shaped central hot void has developed in the central meridional cross-section (as is shown in the middle and bottom rows of Figure 4 for $t = 18.24$ hr and $t = 23.79$ hr), the strongest portion of the current layer has become a central inverse S-shaped vertical layer underlying the flux rope (see the middle and right panels of Figure 5 and the associated movie in the online version). The inverse-S shape is consistent with the left-handed twist of the flux rope (e.g., Fan & Gibson 2004). A

forward-S shape for the current layer would result for a right-hand-twisted flux rope.

We find that these current layers in the simulation (as shown in Figure 5) develop along topological structures identified as quasi separatrix layers (QSLs), which are regions of the magnetic volume where the field line connectivity experiences drastic variations (Démoulin et al. 1996a, 1996b; Titov et al. 2002). They are a generalization of the concept of separatrices at which the field line linkage is discontinuous. Similar to a separatrix, a QSL divides the coronal domain into quasi-connectivity domains, and due to the drastic change of the field
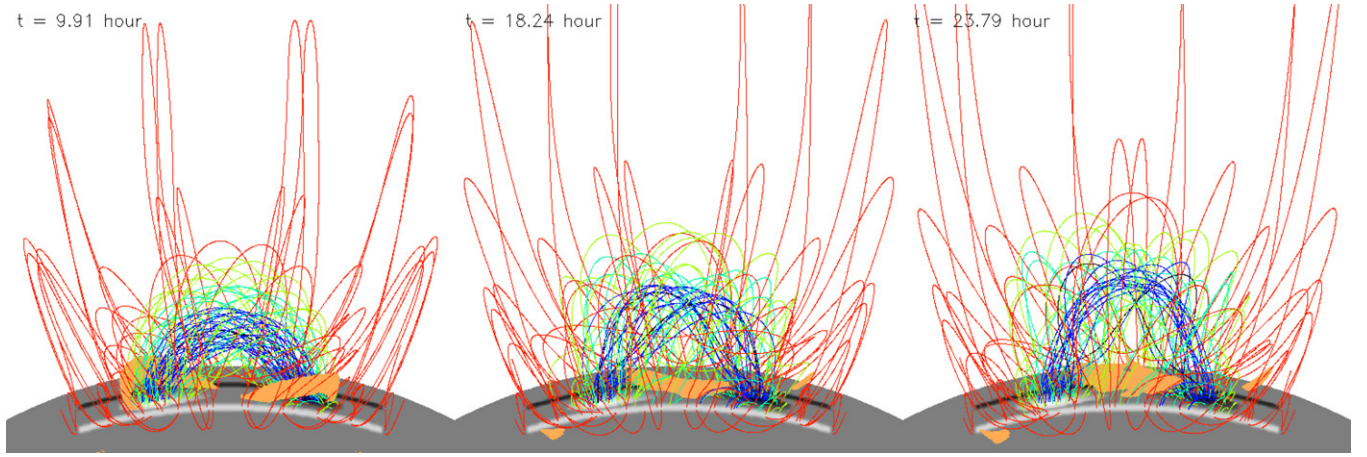
Figure 5. 3D coronal field lines and the iso-surface of J/B at a value of $1/(10\,dr)$ where dr is the smallest grid size in r at times $t = 9.91$ hr, $t = 18.24$ hr, and $t = 23.79$ hr. An animation of the 3D structures with a rotating perspective is also available in the online version of the paper.

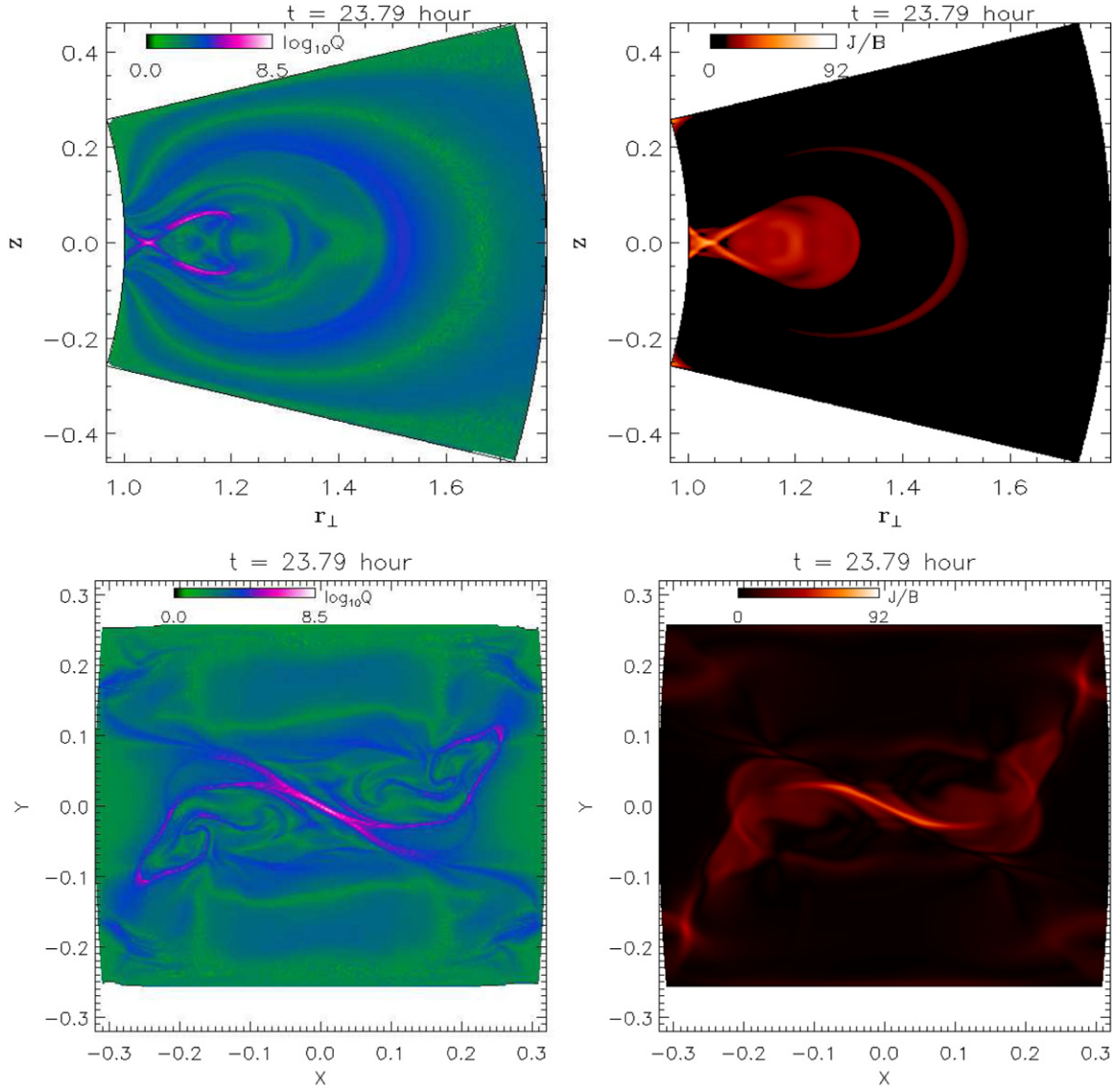(An animation of this figure is available in the online journal.)

Figure 6. Estimation of the squashing degree Q in, respectively, the central meridional cross-section (upper left panel) and the cross-section at the height of $r = 1.048\,R_\odot$ (lower panel) in the 3D magnetic field shown in the right panel of Figure 5, and the corresponding 2D cuts of J/B (right panels).
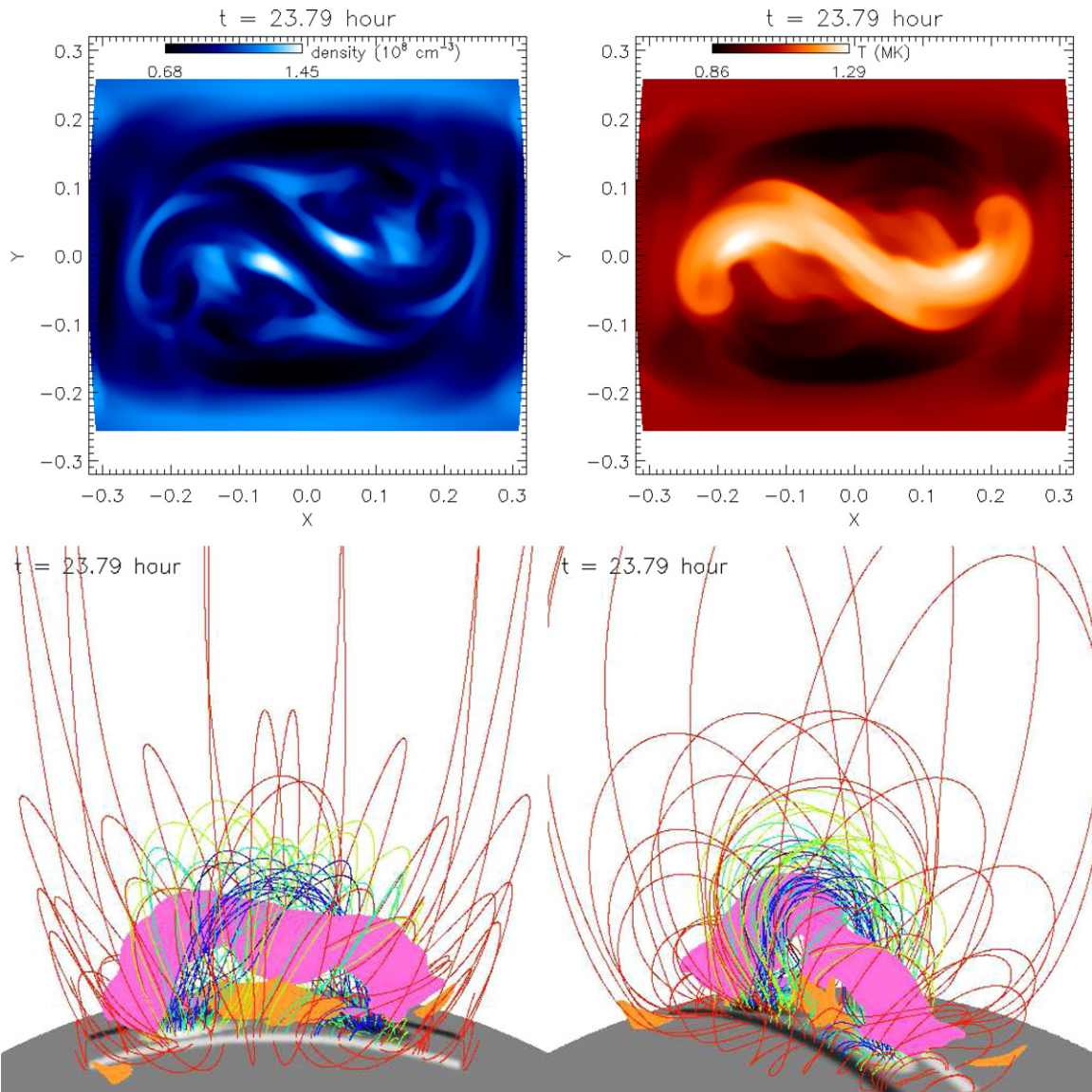
Figure 7. Top panels show the horizontal cross-sections of density and temperature at $r = 1.15\,R_\odot$ for $t = 23.79$ hr, corresponding to the height indicated by the green arrows in the bottom row of Figure 4. The lower panels show two perspective views of the 3D magnetic field lines, the pink iso-surface of temperature at 1.2 MK, which outlines the central hot channel, and the current layers outlined by the orange iso-surfaces of J/B at the level of $1/(10dr)$, with dr being the smallest radial grid size. A movie showing the rotating view of the 3D structures in the lower panels is available in the online version of the paper.

(An animation of this figure is available in the online journal.)

line connectivity, it is a site along which thin and intense current sheets tend to build up because of the distinct dynamic behaviors and evolutions of the field lines in each of these subdomains in the line-tied corona (e.g., Démoulin et al. 1996b; Aulanier et al. 2005; Savcheva et al. 2012a). QSLs are located by estimating the so-called squashing degree, Q, which is defined as the square of the norm of the Jacobian matrix of the field line mapping from one footpoint to the other, divided by the absolute value of the determinant of the Jacobian matrix (Titov et al. 2002; Titov 2007; Pariat & Démoulin 2012). QSLs correspond to regions of very large Q, larger than the averaged values of the rest of the domain by many orders of magnitude (e.g., Pariat & Démoulin 2012; Savcheva et al. 2012a). We have evaluated the squashing degree Q in our simulated coronal magnetic field using the formulation described in Pariat & Démoulin (2012, method 3 in the paper). The left panels in Figure 6 show the computed Q in respectively the central meridional cross-section (upper panel)

and the cross-section at the height of $r = 1.048\,R_\odot$ (lower panel) in the 3D magnetic field shown in the right panel of Figure 5. Compared to the corresponding two-dimensional (2D) cuts of J/B shown in the right panels of Figure 6, we can see that the thin, most intense current layers indeed form along the QSLs with the largest Q values, which are orders of magnitude greater than the averaged Q in the rest of the domain. The QSLs with the highest Q values shown in the central meridional cross-section (top left panel of Figure 6) correspond to the mid cross-section of the so-called Hyperbolic Flux Tube (HFT), a generalization of the X-line configuration, which divides the magnetic volume into four distinct domains of magnetic field connectivity (e.g., Titov 2007; Aulanier et al. 2005; Savcheva et al. 2012a). The main central vertical current layer shown in the right panel of Figure 5 (whose cross-sections are shown in the 2D cuts in Figure 6) forms along the HFT and is likely a thin current sheet that can lead to significant reconnection even
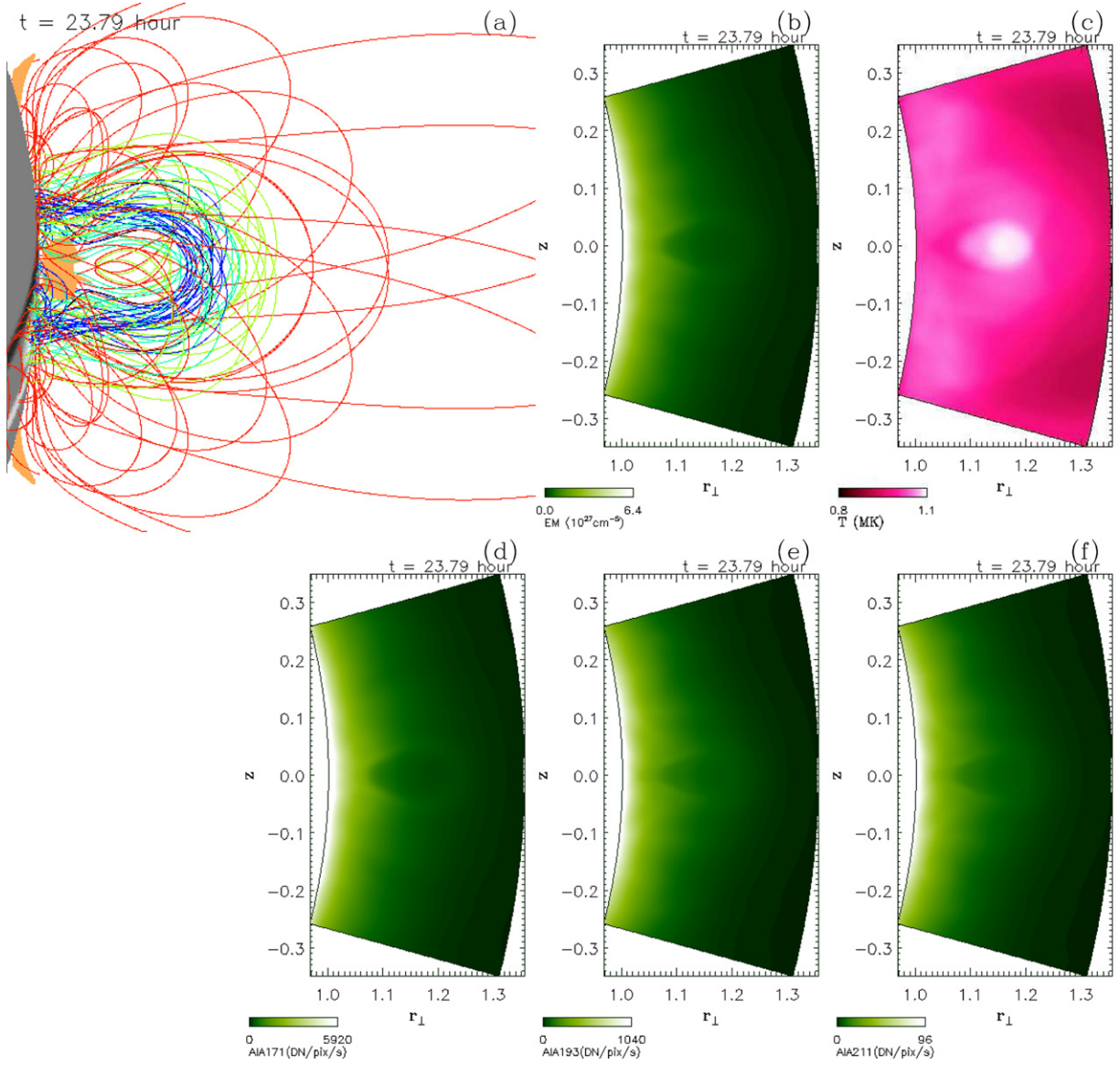
Figure 8. (a) The 3D field lines and the iso-surface of J/B at a value of $1/(10\,dr)$ with dr being the smallest radial grid size, viewed above the limb along the line of sight that is tilted by $40°$ clockwise from the east–west direction (or the direction of the axis of the flux rope). Also shown are modeled images of the emission measure (b), line-of-sight-averaged temperature (c), and SDO/AIA intensities at 171 Å (d), 193 Å (e), and 211 Å (f) channels, by integrating through the simulation domain along the same line of sight.
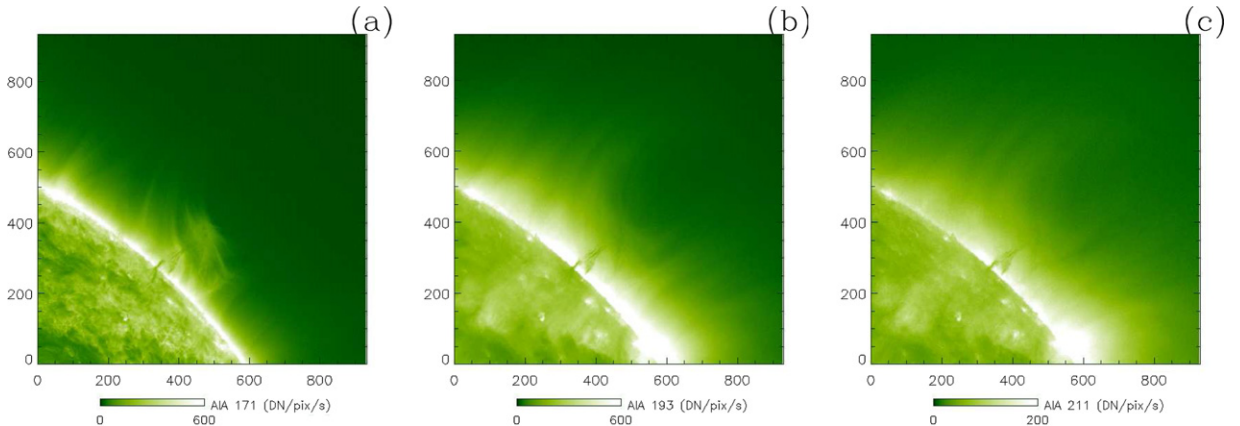

Figure 9. Prominence cavity observed by SDO/AIA on 2012 June 12 at about 23:01 UT on the northwest limb. See also Figure 1 of Régnier et al. (2011) which shows sharper inverse-color images of the same cavity at a later time on 2012 June 13 at about 03:36 UT.
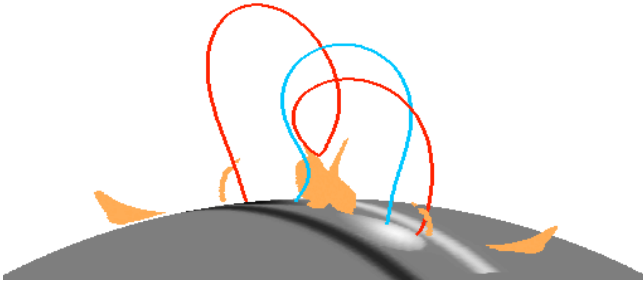
t=23.79 hour

(a)   t=9.91 hour   (b)   t=23.79 hour

Figure 10. 3D view of the current layers as outlined by the iso-surface of J/B at a value of $1/(10dr)$, with dr being the smallest radial grid size, and two field lines traced from two points in close proximity on opposite sides of one of the upward extensions of the central vertical current layer.

(An animation of this figure is available in the online journal.)
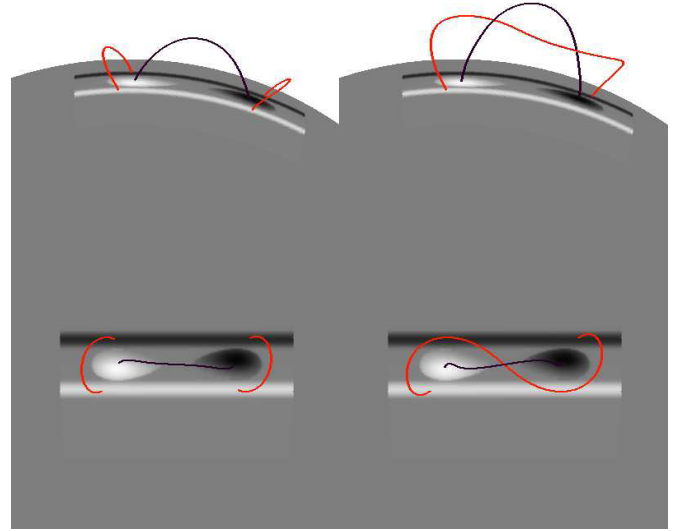
Figure 11. 3D views of selected field lines from two perspectives. Black field lines are the tracked axis of the flux rope. The red field lines are field lines traced from two fixed footpoints in the arcade region. At $t = 9.91$ hr, the red field lines are two simple arcade loops. At $t = 23.79$ the red field line traced from the same two footpoints in the arcade region has become a field line that threads under and twists about the axis of the flux rope, and it goes through the central hot void.

under the realistic high Lundquist number condition of the solar corona.

To understand the 3D structure of the growing central hot void on top of the central vertical current layer seen in the cross-sections in Figure 4, we show in the top panels of Figure 7 the horizontal cross-sections of density and temperature at $r = 1.15\,R_\odot$ for $t = 23.79$ hr (corresponding to the height indicated by the green arrows in the bottom row of Figure 4). We see a hot channel of inverse-S shape, with the main middle segment of the channel tilted away from the east–west direction (or the direction of the emerging flux rope axis) clockwise by roughly $40°$. There is a good anti-correlation between the temperature and the density of the channel, i.e., it is a hot, low-density channel. In the lower panels of Figure 7, we also show the 3D morphology of the hot channel as outlined by the pink isosurface of temperature (at 1.2 MK) in relation to the current layers (orange isosurfaces of J/B) and the magnetic field lines. The hot channel is on top of the central vertical current layer, and the current layer extends upward to surround the two sides of the hot channel in the middle portion (see the movie associated with Figure 7 in the online version which show the rotating view of the 3D structures). The hot channel also threads under the axial field line of the flux rope (as indicate in the bottom panels of Figure 4).

If this flux rope is viewed above the limb, with a line of sight that is aligned with the main middle segment of the hot channel to a suitable angle, then one would be able to observe the central void of high temperature inside the flux rope. Figure 8 shows the modeled images above the limb of the emission measure (panel (b)), line-of-sight-averaged temperature (panel (c)), and SDO/AIA intensities for the 171 Å (panel (d)), 193 Å (panel (e)), and 211 Å (panel (f)) filters, by integrating through the simulation domain along the line of sight that is tilted $40°$ clockwise from the east–west direction (or the direction of the axis of the flux rope). Also shown in the figure is the view above

the limb of the 3D field lines and the iso-surface of J/B (at a value of $1/10\,dr$ with dr being the smallest radial grid size) along the same line of sight (Figure 8(a)). For computing the modeled emission above the limb at the AIA 171 Å, 193 Å, and 211 Å wavelength channels, we use the temperature and density from the simulation and carry out the following integration along the line-of-sight l through the domain:

$$I_i = \int n_e^2(l)\, f_i(T(l), n_e(l))\, dl, \qquad (18)$$

where the subscript i denotes one of the AIA wavelength channels, I_i denotes the intensity at each pixel in units of DN/s/pixel, n_e is the electron number density, and the function $f_i(T, n_e)$ takes into account the atomic physics and the properties of the AIA filters. We have ignored the weak dependence of f_i on n_e and obtained the temperature-dependent function $f_i(T)$ using the SolarSoft routine `get_aia_response.pro`.

The resulting modeled emission measure and the AIA intensity images in Figure 8 show a central tear-shaped void with a relatively sharp U-shaped lower boundary, surrounded by a relatively dense shell. The central tear-shaped void is the central low-density, hot channel viewed along its main part of the length (see Figure 7), and the U-shaped dense shell enclosing the void is produced by the upward extensions of the vertical current layer (see the orange isosurfaces in Figure 8(a)) which has formed along the HFT. Note that the tear-shaped void enclosed by a U-shaped dense shell on top of a vertical dense structure is inside the larger flux rope structure. Such a central density sub-structure inside the flux rope has been observed in some of the quiescent prominence cavities at the limb (e.g., Régnier et al. 2011; Reeves et al. 2012; Berger 2012). Figure 9 shows a prominence cavity observed by SDO/AIA on 2012 June 12 at about 23:01 UT on the northwest limb.
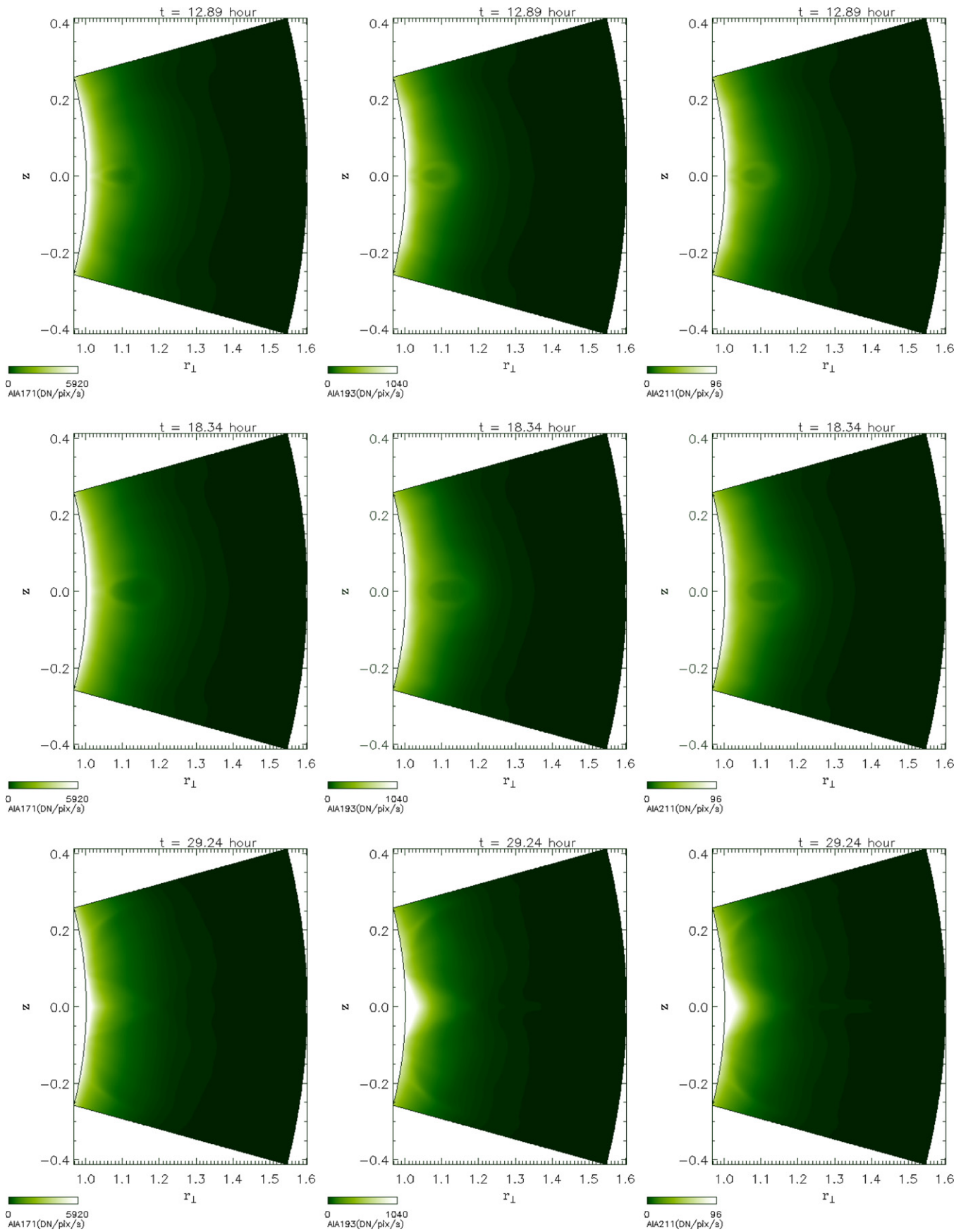
Figure 12. Snapshots of the modeled AIA intensity images at 171 Å, 193 Å, and 211 Å channels at three time instances, showing the expansion and rise of the central void during the quasi-static phase, and its final ejection and the post eruption brightening.

(An animation of this figure is available in the online journal.)

This is also the case studied by Régnier et al. (2011, see also Figure 1 in that paper for the sharper negative images). The AIA 171, 193, 211 images all show an ellipse-shaped central void with a sharp U-shaped lower boundary situated on top of the vertical prominence. The void is enclosed by a U-shaped dense shell extending upward from the prominence. These qualitative features are similar to those seen in the modeled AIA images shown in Figure 8, provided that the observed prominence material is co-spatial with the vertical current layer in the model (Figure 8(a)). Prominence condensation may develop inside the denser current layer due to radiative cooling, which is not included in our numerical simulation. The U-shaped dense shell extending upward from the prominence seen most prominently in the AIA 171 observations is also called "horns" (Berger 2012) and is found to be common features of quiescent prominences observed with the AIA. Our model suggests that this observed density feature of a dense prominence column with upward extending horns corresponds to the current sheet that forms along the HFT, when viewed from a suitable line-of-sight angle, as illustrated by Figure 10, which can be compared qualitatively with the prominence and horn morphology shown in Figure 3 of Berger (2012). In other words, the development of a dense prominence column with upward extending horns enclosing a central void (such as the cases shown in Régnier et al. 2011 and Berger 2012) signifies the development of the HFT topology (and the associated tether-cutting reconnections) in the cavity flux rope. Figure 10 also shows two field lines drawn from two points in close proximity on opposite sides of one of the upward extensions of the central current layer. It illustrates the drastic difference in the connectivities of these two field lines which come to close proximity on opposite sides of the current layer extension (which is a QSL) with very different field line orientations. A 3D rotating view of the current layer and the field lines is available as a movie associated with Figure 10 in the online version.

The anti-correlation between the emission measure and the temperature for the central void structure (Figures 8(b) and (c)) is also consistent with the recent study of internal thermal properties of coronal cavities by Reeves et al. (2012). They found a central core with lower density but higher temperature inside the larger coronal cavity. This central hot core is also consistent with the X-ray emitting core sometimes observed in coronal cavities (e.g., Hudson et al. 1999; Reeves et al. 2012).

Our model suggests that this sub-structure of the hot, low-density channel inside the larger flux rope corresponds to the reconnected, twisted flux being added to the flux rope via tether-cutting reconnections in the current layers which have formed along the HFT during the quasi-static stage (see orange surfaces in Figure 5). Figure 11(b) illustrates such a reconnected field line through the central hot void (see the red field line), which at $t = 23.79$ hr has become a field line that twists about the tracked axis (black field line) of the flux rope. Yet, this red field line has its footpoints rooted in the arcade regions. At an earlier time $t = 9.91$ hr (see Figure 11(a)), the field lines drawn from these footpoints are two simple arcade field lines (the red field lines in Figure 11(a)). Thus, the two simple arcade field lines at $t = 9.91$ hr have undergone multiple reconnections with the flux rope fields, and by time $t = 23.79$ hr have turn into a field line rooted in the arcade footpoints but twists about the axis of the flux rope. Such addition of the twisted flux to the flux rope, threading under the axis, produces the expanding, low-density hot channel in the flux rope. When viewed in a line of sight that is roughly aligned with the channel, the resulting central void

is found to enlarge and rise up during the quasi-static stage (see Figure 12 and the associated movie in the online version of the paper). As the critical height is reached, the central void accelerates rapidly upward and is ejected, leaving behind a cusp-shaped brightening (see the last row in Figure 12). The development of the long bright current sheet trailing the ejected central void (see the movie) and the rise of the cusp-shaped brightening are more prominent in the 193 and 211 channels due to their sensitivity to higher temperatures. This evolution sequence can be compared with the observed evolution of the prominence cavity studied in Régnier et al. (2011), which begins to erupt at about 03:24 UT on 2010 June 13. A composite movie of the AIA observation in the 171, 193, and 211 channels of the evolution of this cavity on the northwest limb during the period from 18:00 UT 2010 June 12 to 21:30 UT 2010 June 13 can be viewed at http://sdowww.lmsal.com/suntoday/index.html?suntoday_date=2010-06-12#. The observed evolution shows many qualitative similarities with the modeled one, including the morphology of the central void enclosed in the U-shaped dense shell on top of a dense column during the quasi-static phase, and the ejection of the void and the post-eruption brightening.

4. CONCLUSIONS

We have carried out an MHD simulation of the quasi-static rise and the onset of eruption of an anchored coronal flux rope. Earlier in the simulation, the emergence of a twisted flux rope is imposed at the lower boundary into a pre-existing coronal potential arcade field. Then the emergence is stopped at the lower boundary and the coronal magnetic field is allowed to settle into a quasi-static equilibrium. It is found that the flux rope first settles into a quasi-static rise phase with an underlying sigmoid-shaped current layer developing along the HFT, which is argued to be a likely site for the formation of thin current sheets and magnetic reconnections (e.g., Titov 2007; Aulanier et al. 2005; Savcheva et al. 2012a). Tether-cutting reconnections in the current layer effectively add twisted flux to the flux rope and allow it to rise quasi-statically (even as the free magnetic energy is decreasing) and the flux rope undergoes dynamic eruption when it reaches the critical height for the onset of the torus instability (Aulanier et al. 2010; Fan 2010). In the present simulation, we study the thermal signatures that result from the development of the HFT topology and the associated tether-cutting reconnections in the current sheets that form along the HFT. We solve the total energy equation in conservative form for a perfect gas with an adiabatic index $\gamma = 1.1$ and thus incorporate the non-adiabatic heating resulting from the dissipation of kinetic and magnetic energies due to the formation of intense current layers. Furthermore, thermal conduction along magnetic field lines is also included in the energy equation so as to incorporate the redistribution of heat along the field lines. In this way, we are able to identify qualitatively the thermal signatures in the flux rope due to heating produced by the tether-cutting reconnections in the current layers that form during the quasi-static rise phase of the flux rope

Intense current layers are found to develop during the quasi-static phase along QSLs, which are topological boundaries where the magnetic field connectivity undergoes drastic variations and are likely sites for the formation of thin current sheets and significant magnetic reconnections (Démoulin et al. 1996a, 1996b; Titov et al. 2002). This has been shown also in previous MHD simulations of coronal flux rope evolution as well as nonlinear force-free field (NLFFF) models of observed sigmoid active regions (e.g., Aulanier et al. 2005, 2010; Savcheva et al.

2012b, 2012a). The strongest portions of the current layers that form are initially two J-shaped layers curving about the two legs of the flux rope at the boundaries between the flux rope legs and the arcade with the opposite polarity footpoints (see the left panel of Figure 5). Later the strongest portion of the current layer becomes a central inverse S-shaped vertical layer that forms along the HFT (see the right panel of Figure 5 and the 2D cuts shown in Figure 6). Reconnections in the current layers are found to add to the flux rope twisted flux threading under the axis, creating an expanding, low-density hot channel in the flux rope above the central vertical current layer. When viewed along a line of sight that is roughly aligned with the channel, it manifests as a central hot void on top of a relatively dense structure corresponding to the central warped, vertical current layer, which also extends upward on two sides of the void (see the J/B image at $t = 18.24$ hr in Figure 4), producing the U-shaped dense shell (or horns) enclosing the void in the modeled EUV images (see, e.g., the $t = 12.89$ hr and $t = 18.34$ hr panels of the modeled AIA 171 images in Figures 12). The dense vertical column and the upward extended horns are essentially the manifestation of the HFT (see the 2D cut in the top left panel of Figure 6). Such thermal structures inside the flux rope are consistent with several AIA EUV observations of coronal prominence cavities where it is found that an elevated, ellipse, or tear-shaped central void is situated on top of the vertical column of dense prominence, and the void is enclosed by a U-shaped dense shell (sometimes called horns) extending upward from the prominence column (e.g., Régnier et al. 2011; Berger 2012). The central hot channel produced by the tether-cutting reconnections can also explain the observational result of a central hot core with low emission measure inside a coronal cavity by Reeves et al. (2012).

Although our numerical simulation does not include radiative cooling and thus cannot model the process of prominence formation, it is likely that the prominence plasma is co-spatial with the dense current layer (e.g., van Ballegooijen & Cranmer 2010; Low et al. 2012). Our MHD simulation also does not model explicitly the background coronal heating but instead simply assumes a high temperature coronal plasma with an adiabatic index of $\gamma = 1.1$, without explicitly incorporating the coronal heating and radiative cooling processes. However, our model does take into account localized heating due to the formation and dissipation of current sheets in the corona and the redistribution of the heat by field aligned conduction in the corona. The lower boundary of our simulation domain is placed at the coronal base instead of the chromosphere, and after the emergence is stopped, the velocity field is set to zero on the lower boundary and no more mass flux is allowed through it into the coronal domain. This precludes the important effect of chromospheric evaporation due to conductive heat flux coming down from the corona, which may significantly affect the density of the heated coronal flux tubes. Thus, there are great uncertainties in the density and temperature obtained due to our still highly simplified treatment of the thermodynamics, especially for the heated, twisted field lines in the hot channel that form as a result of the tether-cutting reconnections. One main question would be whether the heated field in the hot channel would remain a void (i.e., of lower density) in contrast to the surrounding as is in our model when the effect of chromospheric evaporation produced by the downward heat conduction is taken into account. In regard to this question, one consideration is that the reconnected field lines in the hot channel are generally long field lines (see, e.g., the red field lines

in panel 11(b) and Figure 10). The scaling law derived based on the static, thermal equilibrium coronal loop model of Rosner et al. (1978) gives $T_{max} \sim 1.4 \times 10^3 (pL)^{1/3}$, where T_{max}, p, and L denote, respectively, the maximum loop temperature, the loop pressure, and the loop length. This would mean that the plasma density of the loop $\rho \propto T_{max}^2 L^{-1}$. Thus even though the field lines in the hot core are heated to a mildly increased T_{max}: to roughly 1.2 MK from the 1 MK original coronal temperature, these field lines are on the other hand considerably longer in L compared to the field lines immediately outside the hot core: for example, in Figure 10, the red field line inside the central void is about 1.9 times the blue field line immediately outside of the horn. Therefore, the above scaling law of static thermal equilibrium coronal loops would indicate that the effect of the longer length outweighs the effect of the high temperature, and the resulting density inside the central hot channel remains smaller compared to the surrounding, even with the effect of the chromospheric evaporation included.

Our 3D MHD simulations with the simplified thermodynamics are an initial step to understand *qualitatively* the immediate thermal effect of the formation and dissipation of current sheets along the HFT in the corona. Our results suggest that the observed feature of prominence with upward extending horns enclosing an elevated central void seen in AIA 171 observations of coronal cavities is a signature of the development of the HFT topology and the associated tether-cutting reconnections in the current sheets that form along the HFT. It is likely that the current sheet forming along the HFT remains the region of the highest density because of the significant local compression by the Lorentz force even when more realistic treatment of the thermodynamics is included, and our results about the thermal signature, i.e., relatively hot, low-density central void on top of and surrounded by the higher density current sheet formed along the HFT, remain qualitatively true. Of course 3D MHD simulations with a full treatment of the thermal dynamics that incorporates explicit coronal heating, radiative cooling, as well as field-aligned thermal conduction, and with the lower boundary set at the chromosphere, are needed to confirm the findings here and provide quantitative determination of the density and temperature of the coronal plasma. As has been found in one-dimensional hydrodynamic simulations with a full treatment of the thermodynamics along long dipped coronal loops (e.g., Karpen & Antiochos 2008), complex, thermal nonequilibrium formation, and dynamic evolution of prominence condensations can develop along the coronal loops depending on the spatial and temporal properties of the heating profiles prescribed.

Here, we have presented the MHD simulation of the quasi-static evolution and onset of eruption of a particular coronal flux rope configuration. However the results presented here of the development of the HFT topology, and the associated current sheet formation and tether-cutting reconnections along the HFT are quite general results for the evolution of line-tied coronal flux ropes as has been demonstrated by several previous MHD simulations as well as NLFFF models of sigmoid active regions based on observations (e.g., Aulanier et al. 2005, 2010; Savcheva et al. 2012b, 2012a). These models suggest that the development and the elevation of the HFT may be an indication of the extent to which the tether-cutting reconnections have progressed and hence the readiness of the flux rope to erupt.

REFERENCES

Aulanier, G., Pariat, E., & Démoulin, P. 2005, A&A, 444, 961
Aulanier, G., Török, T., Demoulin, P., & DeLuca, E. 2010, ApJ, 708, 314
Berger, T. 2012, in ASP Conf. Ser. 463, 2nd ATST-EAST Workshop in Solar Physics: Magnetic Fields from the Photosphere to the Corona, ed. T. Rimmele et al. (San Francisco, CA: ASP), 147
Chen, P. F. 2011, Living Rev. Sol. Phys., 8, 1 (http://www.livingreviews.org/lrsp-2011-1)
Cottaar, M., & Fan, Y. 2009, ApJ, 704, 576
Démoulin, P., & Aulanier, G. 2010, ApJ, 718, 1388
Démoulin, P., Henoux, J. C., Priest, E. R., & Mandrini, C. H. 1996a, A&A, 308, 643
Démoulin, P., Priest, E. R., & Lonie, D. P. 1996b, J. Geophys. Res., 101, 7631
Fan, Y. 2009, ApJ, 697, 1529
Fan, Y. 2010, ApJ, 719, 728
Fan, Y. 2011, ApJ, 740, 68
Fan, Y., & Gibson, S. E. 2004, ApJ, 609, 1123
Fan, Y., & Gibson, S. E. 2007, ApJ, 668, 1232
Forbes, T. G., Linker, J. A., Chen, J., et al. 2006, Space Sci. Rev., 123, 251
Gibson, S. E., & Fan, Y. 2006, J. Geophys. Res., 111, A12103
Hudson, H. S., Acton, L. W., Harvey, K. L., & McKenzie, D. E. 1999, ApJ, 513, L83
Isenberg, P. A., & Forbes, T. G. 2007, ApJ, 670, 1453
Karpen, J. T., & Antiochos, S. K. 2008, ApJ, 676, 658
Kliem, B., & Török, T. 2006, Phys. Rev. Lett., 96, 255002
Low, B. C. 2001, J. Geophys. Res., 10625141
Low, B. C., Berger, T., Casini, R., & Liu, W. 2012, ApJ, 755, 34
Low, B. C., & Zhang, M. 2002, ApJ, 564, L53
Pariat, E., & Démoulin, P. 2012, A&A, 541, A78
Reeves, K. K., Gibson, S. E., Kucera, T. A., Hudson, H. S., & Kano, R. 2012, ApJ, 746, 146
Régnier, S., Walsh, R. W., & Alexander, C. E. 2011, A&A, 533, L1
Rempel, M., Schüssler, M., & Knölker, M. 2009, ApJ, 691, 640
Rosner, R., Tucker, W. H., & Vaiana, G. S. 1978, ApJ, 220, 643
Savcheva, A., Pariat, E., van Ballegooijen, A., Aulanier, G., & DeLuca, E. 2012a, ApJ, 750, 15
Savcheva, A., van Ballegooijen, A. A., & DeLuca, E. E. 2012b, ApJ, 744, 78
Stone, J. M., & Norman, M. L. 1992a, ApJS, 80, 753
Stone, J. M., & Norman, M. L. 1992b, ApJS, 80, 791
Titov, V. S. 2007, ApJ, 660, 863
Titov, V. S., & Demoulin, P. 1999, A&A, 351, 707
Titov, V. S., Hornig, G., & Démoulin, P. 2002, J. Geophys. Res., 107, 1164
Török, T., & Kliem, B. 2007, Astron. Nachr., 328, 743
van Ballegooijen, A. A., & Cranmer, S. R. 2010, ApJ, 711, 164
Wang, Y.-M., & Stenborg, G. 2010, ApJ, 719, 181